Structural bases of the altered catalytic properties of a pathogenic variant of apoptosis inducing factor

Luca Sorrentino[a, b]❖, Federica Cossu[a, b]❖, Mario Milani[a, b], Alessandro Aliverti[b]*, Eloise Mastrangelo[a, b]**

[a]Biophysics Institute, National Research Council c/o Department of Biosciences, Università degli Studi di Milano, Via Celoria 26, 20133 Milano, Italy;

[b]Department of Biosciences, Università degli Studi di Milano, via Celoria 26, 20133 Milano, Italy.

❖LS and FC contributed equally to this work.

* To whom correspondence should be addressed:

Phone: +39 0250314897.

Fax: +39 0250314895.

E-mail: alessandro.aliverti@unimi.it

** To whom correspondence should be addressed:

Phone: +39 0250314898.

Fax: +39 0250314895.

E-mail: eloise.mastrangelo@unimi.it

1

Abbreviations

AIF^{CT}, AIF forms in CT complex with NAD$^+$;

AIF^{OX}, AIF forms harboring oxidized FAD;

CHCHD4, coiled-coil-helix-coiled-coil-helix domain-containing protein 4;

CT, charge transfer;

DCIP, 2,6-dichlorophenolindophenol;

FADH$^-$, anionic dihydroquinone form of FAD;

OXPHOS, oxidative phosphorylation.

Abstract

The apoptosis-inducing factor (AIF) is a FAD-containing protein playing critical roles in caspase-independent apoptosis and mitochondrial respiratory chain biogenesis and maintenance. While its lethal role is well known, the details of its mitochondrial function remain elusive. So far, nineteen allelic variants of AIF have been associated to human diseases, mainly affecting the nervous system. A strict correlation is emerging between the degree of impairment of its ability to stabilize the charge-transfer (CT) complex between FAD and NAD^+ and the severity of the resulting pathology. Recently, we demonstrated that the G307E replacement in murine AIF (equivalent to the pathogenic G308E in the human protein) dramatically decreases the rate of CT complex formation through the destabilization of the flavoprotein interaction with NAD(H). To provide further insights into the structural bases of its altered functional properties, here we report the first crystal structure of an AIF pathogenic mutant variant in complex with NAD^+ (murine AIF-G307E^{CT}) in comparison with its oxidized form. With respect to wild type AIF, the mutation leads to an altered positioning of NAD^+ adenylate moiety, which slows down CT complex formation. Moreover, the altered balance between the binding of the adenine/nicotinamide portions of the coenzyme determines a large drop in AIF-G307E ability to discriminate between NADH and NADPH.

The apoptosis inducing factor (AIF) [1, 2] is a mitochondrial flavoprotein, highly conserved in vertebrates and with homologs in most eukaryotes [2, 3]. It is encoded by the *AIFM1* gene on the X chromosome and translated as a precursor apoprotein with an N-terminal mitochondrial localization sequence (MLS) and two nuclear localization signals (NLS) [4]. The mature form of the protein, AIFΔ1-54, is tethered to the intermembrane side of mitochondrial inner membrane *via* its N-terminal segment [1]. As other mitochondrial proteins, AIF has a role in programmed cell death, being the main mediator of caspase-independent apoptosis [1, 2]. Apoptotic stimuli can produce the soluble AIFΔ1-102 form, which is released into the cytosol [5, 6] and, if translocated into the nucleus, can bind DNA to promote chromatin condensation and large-scale DNA degradation [7]. However, AIF is also critical for the integrity of mitochondria in healthy cells [5, 8, 9]. Down-regulation of *AIFM1* expression impairs oxidative phosphorylation (OXPHOS), mainly affecting complexes I and III [5, 10], suggesting that AIF has a function in respiratory chain biogenesis and/or maintenance [2]. This hypothesis is supported by the recent discovery that AIF is required for the translation-coupled import and activity of CHCHD4 [11], an intermembrane mitochondrial space protein that participates to the oxidative folding of respiratory complexes subunits [12].

Most of the molecular mechanism by which AIF assists mitochondrial structure and functions still remains elusive. However, AIF interaction with NAD(H) seems to be pivotal for the vital functions of the flavoprotein [2, 13]. NAD(H)-binding to AIF yields an exceptionally oxygen-stable $FADH^-\text{-}NAD^+$ charge-transfer complex (AIF^{CT}) that leads to large conformational rearrangements and dimerization of the protein [13-15]. These features led to the hypothesis that AIF could represent a redox and/or NADH sensor, taking part to a novel signal-transduction pathway [2,

13]. Moreover, AIF^{CT} formation and protein dimerization are known to prevent its nuclear localization, to weaken its interaction with DNA and to hamper interactions with pro-survival cytoplasmatic partners [13].

OXPHOS defects are typically associated with neurodegeneration [16]. Both the Harlequin mouse, a natural murine strain where AIF level is decreased by 80%, and experimental models of AIF deficiency display OXPHOS defects, mitochondrial alterations and neuron loss [2, 9]. To date, nineteen human pathogenic AIF allelic variants have been identified, eleven of which associated with auditory neuropathy spectrum disorders [17], and the others causing neurodegenerative diseases of different degrees of severity [18-25]. Among the latter group, we focused our attention on the G308E replacement, responsible of a rare mitochondrial encephalopathy [19]. We have recently reported the thorough biochemical characterization of murine AIF-G307E, equivalent to human AIF-G308E, demonstrating that this replacement selectively slows down the rate of AIF^{CT} formation [26]. The effect of the amino acid replacement on the reaction between the AIF variant harboring oxidized FAD (AIF-G307E^{OX}) and NADH was particularly dramatic, indicating strong destabilization of the initial complex [26]. Our results were fully confirmed by a similar study carried out on the human AIF-G308E variant [27], thus supporting the concept that the mouse homolog is an excellent model of human AIF. While only the crystal structure of the oxidized form of the human AIF-G308E variant has been reported so far [27], we succeeded in determining that of murine AIF-G307E^{CT}, the first CT complex of a pathogenic AIF variant, here described in comparison with the respective oxidized form. We also report new relevant details of the effects of the G307E replacement on the catalytic properties of AIF, which prove that the conformational alterations observed in the crystal are

maintained in solution. These new findings provide a comprehensive picture of the impact of the G307E replacement on the reactivity of AIF towards nicotinamide ligands.

Materials and Methods

Expression and purification of AIF forms. Mouse wild type AIFΔ1-101 and its G307E variant were produced and purified as already described [26]. Purified proteins were stored at -80 °C in 50 mM Tris-HCl (pH 7.4), 10% glycerol, and their concentration was determined spectrophotometrically using an ε_{452} of 12.8 mM^{-1}cm^{-1}.

Crystallization and crystal data collection. Before crystallization trials, dimeric AIF-G307E^{CT} was generated mixing 250 µM (14 mg/mL) oxidized protein with 2.5 mM NADH for 3 h at 0 °C in 100 mM bis-tris propane (pH 7.4). The complex was then isolated by gel filtration on a Superdex 200 column (GE Healthcare) and concentrated to about 12 mg/mL. 1 mM NADH was then added to avoid CT complex reoxidation during crystal growth. Crystals of AIF-G307E^{OX} and AIF-G307E^{CT} were grown at 20 °C in vapour-diffusion set up (Oryx-8 crystallization robot; Douglas Instruments, East Garston, UK) from a 2:1 mixture of protein and reservoir solution (drop volume 0.3 µL). Crystals of AIF-G307E^{OX} were obtained after one day of vapour diffusion against 30% PEG 4000 and 0.2 M sodium acetate (pH 8.5). Crystals of AIF-G307E^{CT} were obtained after one day of vapour diffusion against 10% PEG 6000, 0.1 M HEPES (pH 7.0).

Before data collection, crystals were soaked in cryoprotectant solution containing 20% glycerol and flash-frozen in liquid nitrogen. The X-ray diffraction data were collected at the ESRF beamline ID29 (Grenoble, France) and were indexed and scaled using XDS [28] to a resolution of 3.5 Å and 3.1 Å for the oxidized and reduced forms, respectively.

Structure solution and refinement. The structures of AIF-G307E^{OX} and AIF-G307E^{CT} were solved by the molecular replacement method using the program

MOLREP [29] and the corresponding structures of wild type murine AIF (PDB-ID: 3GD3 and 3GD4, respectively) [14] as search models. For both crystals, the two molecules in the crystal asymmetric unit were subjected to rigid-body refinement, and subsequently to constrained refinement using REFMAC5 [30]. A random set comprising 5% of the data was omitted from refinement for R-free calculation. Manual rebuilding with COOT [31] and additional refinement with BUSTER [32] and REFMAC5 [30] were performed as needed. Buried surface areas and contacts between domains were calculated using PISA [33]. Crystal parameters and data collection statistics for both AIF-G307E^{OX} and AIF-G307E^{CT} are summarized in Table 1. Atomic coordinates and structure factors for the oxidized and CT complex states of AIF-G307E have been deposited in PDB [34], with accession codes 5MIU and 5MIV, respectively. PyMol Graphic System (Schrödinger, LLC) was used for figures preparation.

Kinetic studies. All kinetic measurements were performed using either an 8453 diode-array (Agilent) or an SF-61 DX2 diode-array stopped-flow (HiTech) spectrophotometer. The NADH- or NADPH-dependent 2,6-dichlorophenolindophenol (DCIP) reductase reactions catalyzed by wild type AIF or AIF-G307E were monitored under steady-state conditions at 25 °C in 50 mM Na-phosphate (pH 7.5). For kinetic parameters estimation, the concentration of nicotinamide dinucleotides was varied between 0.1 and 15 mM, while that of DCIP was kept constant at 30 µM. Data fitting was performed as previously reported [26]. The time course of CT complex formation between the AIF forms and NADH or NADPH was monitored after mixing the oxidized proteins with different concentrations of each nucleotide ligand at 25 °C in 50 mM Na-phosphate buffer (pH 7.5). To estimate the parameters of the process, the concentration of NADH or NADPH was varied between 0.02 and

15 mM. Absorbance traces at 450 and 700 nm (specific for AIF-bound oxidized FAD and CT complex, respectively) were fitted to a single exponential decay equation using the software KinetAsyst version 3.0 (Hi-Tech Scientific) to estimate the values of apparent first-order rate constants (k) of the processes [26].

Results

Crystal structures of AIF-G307E. Crystals of AIF-G307E in its oxidized and

CT complex states both belonged to the orthorhombic space group $P2_12_12_1$ with two

molecules per asymmetric unit. As previously reported [35], the protein is composed

of three domains: a FAD-binding domain (residues 122−262 and 400−477), a NADH-

binding domain (residues 263−399) and a C-terminal domain (478−610). Both the

FAD- and NADH-binding domains display the classical Rossmann fold topology,

whereas the C-terminal domain is composed of five antiparallel β-strands followed by

two α-helices. As in all AIF deposited PDB entries, only few electron density

portions of the AIF-G307E regulatory peptide [2] (residues 508-558) are defined

(AIF-G307E^{OX}: residues 508-522; AIF-G307E^{CT}: residues 508-509, 539-543, 557-

558).

Structure of AIF-G307E in its oxidized state. The crystals of AIF-G307E^{OX}

diffracted to a maximum resolution of 3.5 Å, and the structure was refined to a final

crystallographic R-factor of 21.0%, and R-free of 27.8% (Table 1). Structural

superposition of the two independent protein Cα backbones of chain A and B (446

amino acids) yields r.m.s.d. value of 0.5 Å. The superimposition of chain A of the

AIF variant to murine wild type AIF^{OX} (PDB code: 3GD3 [14], r.m.s.d. of 0.7 Å on

453 Cα atoms; Figure 1) pointed out the same differences observed by Sevrioukova

in the corresponding human mutant variant (PDB code: 5FS8) [27]. In particular,

Glu307 lines the wall of the NADH-binding channel and is well ordered, but to

accommodate its bulkier side chain, the nearby Glu335 rotates its χ2 angle by ~180º.

Furthermore, the steric hindrance of the mutated residue causes a ~0.8 Å shift of the

333-335 segment, which affects in cascade the positioning of the 365-370 and the 379-387 portions of the protein.

Structure of AIF-G307E in its CT complex with NAD$^+$. The crystals of AIF-G307E^{CT} diffracted to a maximum resolution of 3.1 Å, and the structure was refined to a final crystallographic R-factor of 19.9%, and R-free of 25.9% (Table 1). As already described for wild type AIF [14], the two molecules in the asymmetric unit (A and C; Figure 2A) are closer than in the structure of oxidized AIF-G307E, thus engaging tighter interactions, the main of which are two intermolecular Glu412-Arg448 salt bridges. Structural superimposition of the two protein Cα backbones (439 amino acids) yields r.m.s.d. value of 0.2 Å. The superimposition of chain A of AIF-G307E^{CT} to murine wild type AIF^{CT} (PDB code: 3GD4 [14]; r.m.s.d. of 1.1 Å) pointed out that all the NADH-driven conformational changes leading to dimeric CT complex formation [14, 15] are conserved in the mutant variant. Fourier maps, at various stages of the crystallographic refinement, revealed strong residual electron density compatible with the NAD$^+$ molecule that was accordingly modeled (Figure 2B-C). As in wild type AIF^{CT}, the nicotinamide ring of the ligand is stacked between FAD isoalloxazine and Phe309 rings (Figure 2C).

The G307E replacement mainly alters the position of the adenylate moiety of bound NAD$^+$ causing its reorientation with a 2 Å shift (Figure 3A). In these conditions, a hydrogen bond between the side chain of Arg264 and NAD$^+$ O2B is established through a water molecule (Figure 3B). The effect of the mutation also affects the protein portion surrounding the NAD$^+$ adenylate moiety, as speculated by Sevrioukova [27]. Compared to AIF-G307E^{OX} structure, a shift of the 332-335 peptide is also observed in AIF-G307E^{CT}, though with no consequences on Glu335

orientation. Nevertheless, such shift leads to the disengagement of Glu335 from its interaction with the adenosine ribose of NAD^+ and to the establishment of a weak electrostatic interaction with the adenine ring (Figure 3B). Furthermore, the repositioning of NAD^+ adenylate moiety causes the severing of the hydrogen bond between the dinucleotide pyrophosphate and Lys341 that becomes involved in a weak interaction with the adenosine ribose (Figure 3B). The complete comparison of the direct interactions between NAD^+ and AIF in the wild type and G307E CT complexes is summarized in Table 2. Overall, the altered conformation of the physiological ligand explains the lower affinity of AIF-G307E for NAD(H) and the dramatic decrease of the rate for CT complex formation [26].

Kinetic studies of AIF-G307E. We speculated that the perturbation of NAD(H) adenylate moiety binding, observed in AIF-G307E^{CT} structure, might result in a decreased ability of the protein to discriminate between NAD(H) and NADP(H). Therefore, we studied the reactivity of both wild type and G307E AIF forms towards NADPH in steady-state and pre-steady state conditions. The K_m^{NADPH} values of the NADPH-DCIP diaphorase reactions catalyzed by both wild type and G307E AIF forms were found so high that only the k_{cat}/K_m^{NADPH} parameter could be estimated with acceptable precision. The catalytic efficiency of both AIF forms towards NADPH was found much lower than that towards NADH (Table 3). Notably, while the G307E replacement decreases k_{cat}/K_m^{NADH} by a factor of 140, it reduces k_{cat}/K_m^{NADPH} only 20-fold. Therefore, the dinucleotide selectivity of AIF, measured as the ratio between k_{cat}/K_m^{NADH} and k_{cat}/K_m^{NADPH}, drops about 6-fold (from about 45 to 7) as a consequence of the mutation. As shown in Table 3, such loss in specificity is also reflected by the kinetics of CT complex formation by reaction of AIF forms with NADH or NADPH. Indeed, the $k_{lim}/K_{0.5}$ ratio of the various reactions closely

approximates the corresponding steady-state k_{cat}/K_m parameter, indicating that, while the reactivity of both AIF forms towards NADH is higher than that towards NADPH, the G307E mutation considerably attenuates such difference.

Discussion

To date, nineteen pathogenic human AIF variants have been discovered, some of which still lack a biochemical characterization. Filling this gap of knowledge is particularly urgent, due to the increasing rate at which new disease-causing AIF variants are emerging. We undertook the detailed study of murine AIF-G307E, demonstrating that this mutation has the selective effect to dramatically decrease the rate of reaction between AIF and NAD(H), possibly due to the impairment of the flavoprotein interactions with the adenylate moiety of the ligand [26]. The new structural and functional findings, here reported, fully corroborate such hypothesis and complete the picture of the consequences of the pathogenic G307E replacement.

With the aim to understand in detail the structural effects of the mutation, we obtained the crystal structure of mouse AIF-G307E in both its oxidized and CT complex states, at 3.5 Å and 3.1 Å resolution, respectively. Even though resolution was not particularly high, the main structural differences leading to the selective effects of the G307E change on protein-NAD^+ interactions have been unambiguously observed. The structural analysis of AIF-G307E^{CT} provides direct evidence that the mutation specifically affects the interaction of AIF with NAD^+ adenylate moiety. In particular, the steric hindrance of Glu307 in the mutant variant causes a shift of the 333-335 peptide and most importantly the different orientation of both Glu335 and Lys341 side chains. Glu335 and Lys341 are pivotal residues in AIF, being involved in important interactions with NAD^+ [14], allowing its correct positioning and the stabilization of the CT complex. A reorientation of NAD^+ adenylate moiety was observed in AIF-G307E^{CT}, as a consequence of all these structural changes.

14

Since wild type AIF is known to display a significant preference for NADH over NADPH [2], we hypothesized that, by hampering the binding of the half of the ligand molecule that differentiates the two dinucleotides, the mutation could alter substrate selectivity of AIF. We thus analyzed the NADPH-dependent DCIP reductase activities of the wild type and G307E AIF forms. As expected, the wild type protein proved to possess a 45-fold higher specificity for NADH in respect to NADPH. This difference was reduced only to 7-fold for AIF-G307E, showing a much lower ability to discriminate between the two nicotinamide dinucleotides. Being CT complex formation the limiting step for AIF redox activity, similar results were obtained by the pre-steady state kinetic study of this pivotal process.

These new structural and functional observations complete our previous thorough biochemical characterization of AIF-G307E [26]. The study here presented could help in paving the way for a full understanding of the vital role that AIF plays in mitochondria and for the future development of therapies to cure threatening diseases associated with its deficiency and/or malfunctioning.

Funding

References

[1] S.A. Susin, H.K. Lorenzo, N. Zamzami, et al., Molecular characterization of mitochondrial apoptosis-inducing factor, Nature, 397 (1999) 441-446.

[2] I.F. Sevrioukova, Apoptosis-inducing factor: structure, function, and redox regulation, Antioxid Redox Signal, 14 (2011) 2545-2579.

[3] H.K. Lorenzo, S.A. Susin, J. Penninger, et al., Apoptosis inducing factor (AIF): a phylogenetically old, caspase-independent effector of cell death, Cell Death Differ, 6 (1999) 516-524.

[4] B.M. Polster, AIF, reactive oxygen species, and neurodegeneration: a "complex" problem, Neurochem Int, 62 (2013) 695-702.

[5] N. Joza, J.A. Pospisilik, E. Hangen, et al., AIF: not just an apoptosis-inducing factor, Ann N Y Acad Sci, 1171 (2009) 2-11.

[6] H. Otera, S. Ohsakaya, Z. Nagaura, et al., Export of mitochondrial AIF in response to proapoptotic stimuli depends on processing at the intermembrane space, EMBO J, 24 (2005) 1375-1386.

[7] S.A. Susin, E. Daugas, L. Ravagnan, et al., Two distinct pathways leading to nuclear apoptosis, J Exp Med, 192 (2000) 571-580.

[8] N. Modjtahedi, F. Giordanetto, F. Madeo, et al., Apoptosis-inducing factor: vital and lethal, Trends Cell Biol, 16 (2006) 264-272.

[9] E. Hangen, K. Blomgren, P. Benit, et al., Life with or without AIF, Trends Biochem Sci, 35 (2010) 278-287.

[10] N. Vahsen, C. Cande, J.J. Briere, et al., AIF deficiency compromises oxidative phosphorylation, EMBO J, 23 (2004) 4679-4689.

[11] E. Hangen, O. Feraud, S. Lachkar, et al., Interaction between AIF and CHCHD4 Regulates Respiratory Chain Biogenesis, Mol Cell, 58 (2015) 1001-1014.

[12] S. Hofmann, U. Rothbauer, N. Muhlenbein, et al., Functional and mutational characterization of human MIA40 acting during import into the mitochondrial intermembrane space, J Mol Biol, 353 (2005) 517-528.

[13] I.Y. Churbanova, I.F. Sevrioukova, Redox-dependent changes in molecular properties of mitochondrial apoptosis-inducing factor, J Biol Chem, 283 (2008) 5622-5631.

[14] I.F. Sevrioukova, Redox-linked conformational dynamics in apoptosis-inducing factor, J Mol Biol, 390 (2009) 924-938.

[15] C.A. Brosey, C. Ho, W.Z. Long, et al., Defining NADH-Driven Allostery Regulating Apoptosis-Inducing Factor, Structure, (2016).

[16] M.E. Breuer, W.J. Koopman, S. Koene, et al., The role of mitochondrial OXPHOS dysfunction in the development of neurologic diseases, Neurobiol Dis, 51 (2013) 27-34.

[17] L. Zong, J. Guan, M. Ealy, et al., Mutations in apoptosis-inducing factor cause X-linked recessive auditory neuropathy spectrum disorder, J Med Genet, 52 (2015) 523-531.

[18] A. Ardissone, G. Piscosquito, A. Legati, et al., A slowly progressive mitochondrial encephalomyopathy widens the spectrum of AIFM1 disorders, Neurology, 84 (2015) 2193-2195.

[19] I. Berger, Z. Ben-Neriah, T. Dor-Wolman, et al., Early prenatal ventriculomegaly due to an AIFM1 mutation identified by linkage analysis and whole exome sequencing, Mol Genet Metab, 104 (2011) 517-520.

[20] D. Diodato, G. Tasca, D. Verrigni, et al., A novel AIFM1 mutation expands the phenotype to an infantile motor neuron disease, Eur J Hum Genet, 24 (2016) 463-466.

[21] D. Ghezzi, I. Sevrioukova, F. Invernizzi, et al., Severe X-linked mitochondrial encephalomyopathy associated with a mutation in apoptosis-inducing factor, Am J Hum Genet, 86 (2010) 639-649.

[22] M. Kettwig, M. Schubach, F.A. Zimmermann, et al., From ventriculomegaly to severe muscular atrophy: expansion of the clinical spectrum related to mutations in AIFM1, Mitochondrion, 21 (2015) 12-18.

[23] H. Mierzewska, M. Rydzanicz, T. Bieganski, et al., Spondyloepimetaphyseal dysplasia with neurodegeneration associated with AIFM1 mutation - a novel phenotype of the mitochondrial disease, Clin Genet, (2016).

[24] E. Pronicka, D. Piekutowska-Abramczuk, E. Ciara, et al., New perspective in diagnostics of mitochondrial disorders: two years' experience with whole-exome sequencing at a national paediatric centre, J Transl Med, 14 (2016) 174.

[25] C. Rinaldi, C. Grunseich, I.F. Sevrioukova, et al., Cowchock syndrome is associated with a mutation in apoptosis-inducing factor, Am J Hum Genet, 91 (2012) 1095-1102.

[26] L. Sorrentino, A.M. Calogero, V. Pandini, et al., Key Role of the Adenylate Moiety and Integrity of the Adenylate-Binding Site for the NAD(+)/H Binding to Mitochondrial Apoptosis-Inducing Factor, Biochemistry, 54 (2015) 6996-7009.

[27] I.F. Sevrioukova, Structure/Function Relations in AIFM1 Variants Associated with Neurodegenerative Disorders, J Mol Biol, 428 (2016) 3650-3665.

[28] W. Kabsch, Xds, Acta Crystallogr D Biol Crystallogr, 66 (2010) 125-132.

[29] A. Vagin, A. Teplyakov, MOLREP: an automated program for molecular replacement, Journal of Applied Crystallography, 30 (1997) 1022-1025.

[30] R.A. Steiner, A.A. Lebedev, G.N. Murshudov, Fisher's information in maximum-likelihood macromolecular crystallographic refinement, Acta Crystallogr D Biol Crystallogr, 59 (2003) 2114-2124.

[31] P. Emsley, B. Lohkamp, W.G. Scott, et al., Features and development of Coot, Acta Crystallogr D Biol Crystallogr, 66 (2010) 486-501.

[32] O.S. Smart, T.O. Womack, C. Flensburg, et al., Exploiting structure similarity in refinement: automated NCS and target-structure restraints in BUSTER, Acta Crystallogr D Biol Crystallogr, 68 (2012) 368-380.

[33] E. Krissinel, K. Henrick, Inference of macromolecular assemblies from crystalline state, J Mol Biol, 372 (2007) 774-797.

[34] H.M. Berman, J. Westbrook, Z. Feng, et al., The Protein Data Bank, Nucleic Acids Res, 28 (2000) 235-242.

[35] M.J. Mate, M. Ortiz-Lombardia, B. Boitel, et al., The crystal structure of the mouse apoptosis-inducing factor AIF, Nat Struct Biol, 9 (2002) 442-446.

Table 1. X-ray data-collection and refinement statistics.

Data collection	AIF-G307E[OX]	AIF-G307E[CT]
Beam line & wavelength (Å)	ESRF ID29 0.97895	ESRF ID29 0.97895
Space group	$P2_12_12_1$	$P2_12_12_1$
Unit-cell parameters (Å)	a=96.0; b=110.1; c=119.6	a=73.4; b=116.8; c=166.5
Molecules in a.u.	2	2
Resolution (Å)	48.7 – 3.5	43.5 – 3.1
Unique reflections	16,448 (1,197)[a]	26,576 (1,946)[b]
Completeness (%)	99.4 (99.8)	99.5 (99.8)
Redundancy	5.4 (5.7)	4.5 (4.7)
Rmeas[†] (%)	39.3 (129.5)	18.8 (127.8)
CC(1/2) (%)	97.3 (73.5)	99.2 (33.1)
Average I/σ (I)	5.3 (1.8)	6.6 (1.3)
Final model		
R factor[‡]/Rfree[§] (%)	21.0/27.8	19.9/25.9
r.m.s. bonds (Å)	0.009	0.010
r.m.s. angles (°)	1.31	1.52
Average protein B fac. ($Å^2$)	73.0	95.0
Residues in most favored regions (%)	94.5%	97.0%
Residues in additionally allowed regions (%)	5.4%	3.0%
PDB-ID	5MIU	5MIV

Values in parentheses are for the highest resolution shell: [a](3.59-3.50), [b](3.18-3.10).

[†] $R_{meas} = (\Sigma (n/(n-1) \Sigma |I - (I)|)/ \Sigma I$ x 100, where I is intensity of a reflection and (I) is its average intensity.

[‡] $R_{factor} = \Sigma |F_o - F_c| / \Sigma |F_o|$ x 100.

[§] R_{free} is calculated on 5% randomly selected reflections, for cross-validation.

Table 2. Distances of AIF-NAD$^+$ direct interactions in the CT complexes engaged by the wild type and G307E protein forms.

Residue	AIF^{CT} (PDB-ID: 3GD4 [14])		AIF-G307E^{CT} (PDB-ID: 5MIV)	
	NAD$^+$ atoms	Mean (Å) ^{a}	NAD$^+$ atoms	Mean (Å) ^{a}
G307/E307	O2B	2.9	O4B	2.9
F309	O2A, O1N	3.1, 3.2	-	
L310	O1N	3.2	O1N	2.8
E313	N7N	2.8	N7N	2.9
E335	O2B, O3B	2.8, 2.8	N3A	3.8
K341	O1A	2.7	O2B	3.2
A396	O4B, O2N	3.7, 3.3	-	
V397	-		N7A	3.5
G398	O2N	2.8	O2N	3.0
E452	O2D, O3D	2.6, 2.6	O2D, O3D	2.7, 2.6
H453	O7N	2.8	O7N	2.9
W482	N7N	2.6	N7N	3.0

^{a} Mean of the distances measured in the two molecules present in the asymmetric unit.

Table 3. Effect of the G307E replacement on the reactivity of AIF towards NADH and NADPH, as evaluated under steady-state and pre-steady state conditions.[a]

AIF form	NADH[b]				NADPH	
	k_{cat}[c]	K_m[c]	k_{cat}/K_m[c]	$k_{lim}/K_{0.5}$[d]	k_{cat}/K_m[c]	$k_{lim}/K_{0.5}$[d]
	(s^{-1})	(mM)	$(M^{-1}s^{-1})$	$(M^{-1}s^{-1})$	$(M^{-1}s^{-1})$	$(M^{-1}s^{-1})$
Wild type	1.38 ± 0.02	1.60 ± 0.08	860 ± 33	550 ± 28	19.0 ± 0.3	25.0 ± 2.2
G307E	0.060 ± 0.001	8.5 ± 0.4	6.7 ± 0.2	7.6 ± 0.4	0.93 ± 0.02	0.90 ± 0.08

[a]All kinetic measurements were determined at 25 °C in 50 mM Na-phopshate (pH 7.5).

[b]Data taken from Sorrentino *et al.* (2015) [26] are shown here for comparison.

[c]Steady-state kinetic parameters of the NADH/NADPH-DCIP diaphorase reaction catalyzed by AIF.

[d]Apparent second-order rate constant of CT complex formation by reaction of oxidized AIF forms with NADH or NADPH.

Figure Legends

Figure 1. The G307E replacement causes local conformational changes in AIF-G307E^{OX}. The structure of AIF-G307E in its oxidized state is shown as magenta cartoons. The 333-336, 365-372, 378-389 peptides of the wild type and G307E AIF forms are shown in grey and cyan, respectively. Electron density for AIF-G307E^{OX} 333-336 segment is shown in cyan. Relevant elements are displayed as sticks: E307 is shown in magenta with dots highlighting the steric hindrance of its side chain; E335 is shown with grey and cyan carbon atoms, for the wild type and G307E AIF forms, respectively; FAD is shown with yellow carbon atoms. Nitrogen, phosphorus and oxygen atoms are shown in blue, orange and red, respectively. Arrows indicate the shifts caused by the G307E mutation.

Figure 2. The dimeric CT complex of AIF-G307E. AIF-G307E dimer is shown in cartoon representation, with molecules A and C in magenta and pink, respectively. Relevant elements are displayed as sticks: FAD carbon atoms are shown in yellow while those of NAD$^+$ and F309 in the color of the corresponding molecule. Nitrogen, phosphorus and oxygen atoms are shown in blue, orange and red, respectively. (A) The dimer formed by molecules A and C in the asymmetric unit. (B) Zoomed view in molecule A, where the green cage shows the Fo-Fc difference Fourier map calculated after few refinement cycles of the protein structure alone. (C) The AIF-G307E-NAD$^+$ CT complex in molecule A.

Figure 3. The G307E replacement alters NAD$^+$ positioning in AIF. The structure of AIF-G307E in its CT complex with NAD$^+$ is shown as magenta cartoons. Nitrogen,

phosphorus and oxygen atoms are shown in blue, orange and red, respectively. (A) The displacement of NAD^+ adenylate moiety in AIF-G307E: FAD is shown in sticks with yellow carbon atoms; NAD^+ is shown in sticks with grey and magenta carbon atoms in the wild type and G307E AIF-NAD^+ CT complexes, respectively; E307 is shown in magenta sticks with the surface of its steric hindrance colored in magenta. (B) The interaction pattern of NAD^+ in AIF-G307E: NAD^+ in the mutant AIF variant is shown as in panel A; residues interacting with the ligand are shown with purple carbon atoms; the water molecule acting as a bridge between R264 and NAD^+ O2B is shown as a light blue sphere; red and green dashed lines represent interactions that are altered or unaltered by the G307E mutation, respectively.
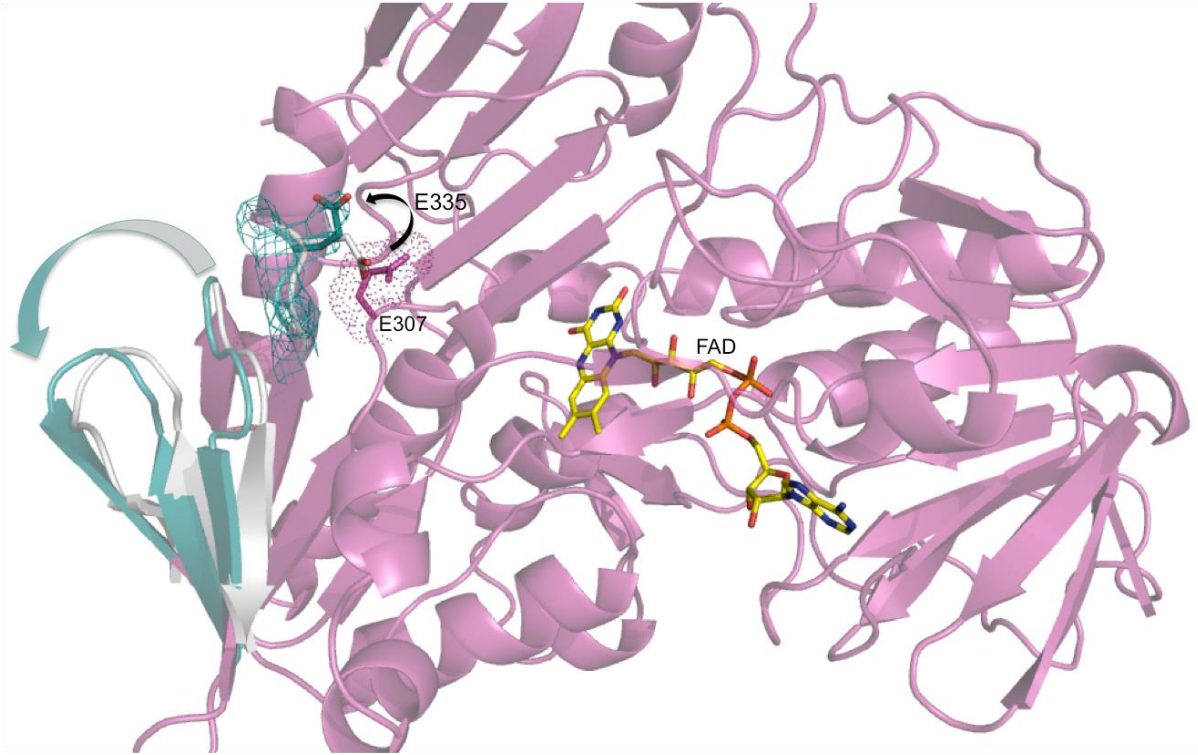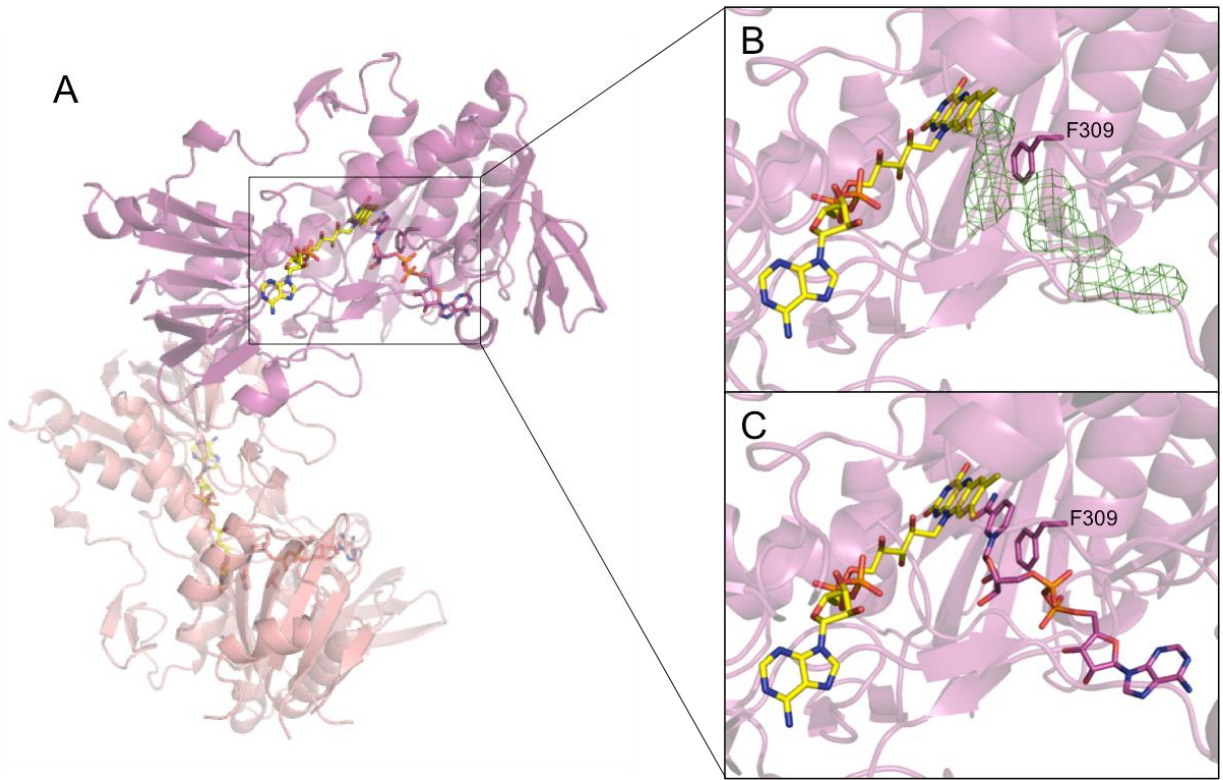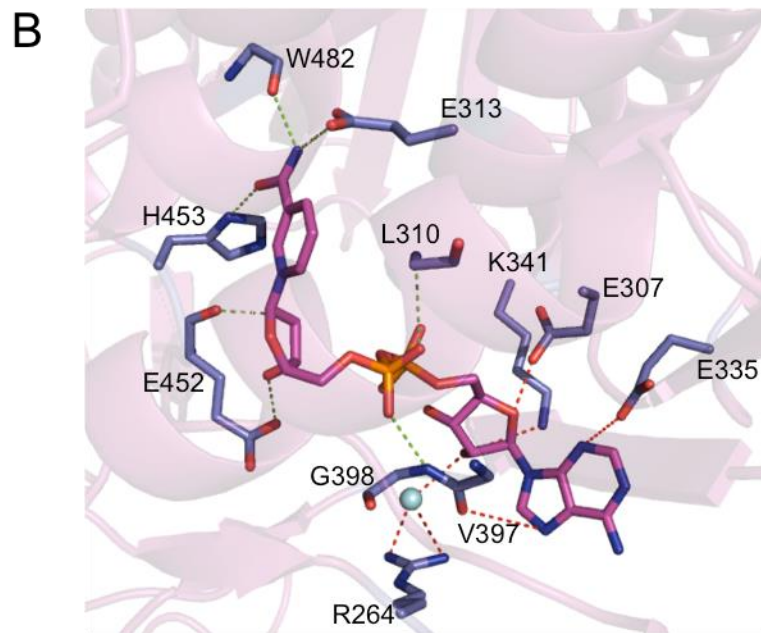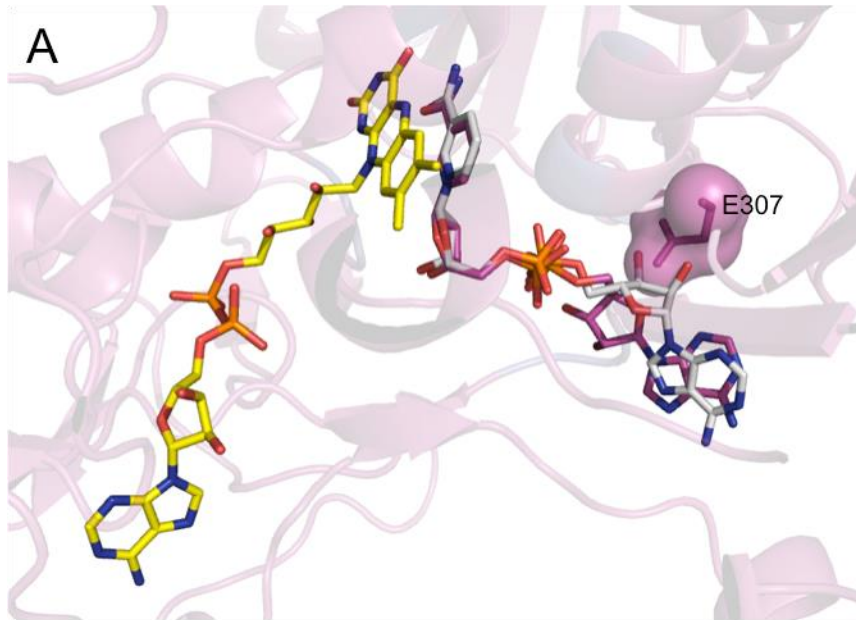
Figure 1

Figure 2

Figure 3